IVYSPRING INTERNATIONAL PUBLISHER

Theranostics

2018; 8(16): 4462-4476. doi: 10.7150/thno.24395

Research Paper

Radionuclide imaging of VEGFR2 in glioma vasculature using biparatopic affibody conjugate: proof-of-principle in a murine model

Bogdan Mitran*[1], Rezan Güler*[2], Francis P. Roche[3], Elin Lindström[1], Ram Kumar Selvaraju[1,4], Filippa Fleetwood[2], Sara S. Rinne[1], Lena Claesson-Welsh[3,5], Vladimir Tolmachev[3], Stefan Ståhl[2], Anna Orlova*[1,5]✉, John Löfblom*[2]

1. Department of Medicinal Chemistry, Uppsala University, Sweden;
2. Department of Protein Science, School of Engineering Sciences in Chemistry, Biotechnology and Health, KTH Royal Institute of Technology, Sweden;
3. Department of Immunology, Genetics and Pathology, Uppsala University, Sweden
4. Preclinical PET-MRI Platform, Department of Medicinal Chemistry, Uppsala University, Sweden
5. Science for Life Laboratory, Uppsala University, Sweden

* These authors contributed equally

✉ Corresponding author: Anna Orlova, Department of Medicinal Chemistry, Uppsala University, Uppsala, Sweden; Address: Dag Hammarskjöldsv 14C, 3tr, 751 83 Uppsala, Sweden; Phone: + 46 18 4715303; FAX: +46 18 4715307 anna.orlova@pet.medchem.uu.se

Received: 2017.12.16; Accepted: 2018.04.21; Published: 2018.08.07

Abstract

Vascular endothelial growth factor receptor-2 (VEGFR2) is a key mediator of angiogenesis and therefore a promising therapeutic target in malignancies including glioblastoma multiforme (GBM). Molecular imaging of VEGFR2 expression may enable patient stratification for antiangiogenic therapy. The goal of the current study was to evaluate the capacity of the novel anti-VEGFR2 biparatopic affibody conjugate (Z_{VEGFR2}-Bp_2) for in vivo visualization of VEGFR2 expression in GBM.

Methods: Z_{VEGFR2}-Bp_2 coupled to a NODAGA chelator was generated and radiolabeled with indium-111. The VEGFR2-expressing murine endothelial cell line MS1 was used to evaluate in vitro binding specificity and affinity, cellular processing and targeting specificity in mice. Further tumor targeting was studied in vivo in GL261 glioblastoma orthotopic tumors. Experimental imaging was performed.

Results: [^{111}In]In-NODAGA-Z_{VEGFR2}-Bp_2 bound specifically to VEGFR2 (K_D=33±18 pM). VEGFR2-mediated accumulation was observed in liver, spleen and lungs. The tumor-to-organ ratios 2 h post injection for mice bearing MS1 tumors were approximately 11 for blood, 15 for muscles and 78 for brain. Intracranial GL261 glioblastoma was visualized using SPECT/CT. The activity uptake in tumors was significantly higher than in normal brain tissue. The tumor-to-cerebellum ratios after injection of 4 μg [^{111}In]In-NODAGA-Z_{VEGFR2}-Bp_2 were significantly higher than the ratios observed for the 40 μg injected dose and for the non-VEGFR2 binding size-matched conjugate, demonstrating target specificity. Microautoradiography of cryosectioned CNS tissue was in good agreement with the SPECT/CT images.

Conclusion: The anti-VEGFR2 affibody conjugate [^{111}In]In-NODAGA-Z_{VEGFR2}-Bp_2 specifically targeted VEGFR2 in vivo and visualized its expression in a murine GBM orthotopic model. Tumor-to-blood ratios for [^{111}In]In-NODAGA-Z_{VEGFR2}-Bp_2 were higher compared to other VEGFR2 imaging probes. [^{111}In]In-NODAGA-Z_{VEGFR2}-Bp_2 appears to be a promising probe for in vivo noninvasive visualization of tumor angiogenesis in glioblastoma.

Key words: VEGFR2, affibody molecule, molecular imaging, SPECT, orthotopic glioma model, in vivo

Introduction

Glioblastoma multiforme (GBM) is the most common and most aggressive primary brain tumor, accounting for more than 50% of all gliomas. Despite aggressive surgery, chemotherapy and radiotherapy, the mean overall survival achieved for GBM patients is less than 18 months [1]. Consequently, substantial

efforts have been made in recent years towards the development of new, improved therapies directed against specific features of the pathology on an individual patient basis. GBM exhibits a highly developed neovasculature and is one of the most vascularized solid tumors. The neovasculature in GBM is heterogeneous, abundant, hyperpermeable, and disorganized with deformed vessels of irregular diameter [2]. The high neovascularization may contribute to the aggressive behavior of GBM, and the inhibition of tumor angiogenesis is a promising therapeutic strategy.

A vast network of pro-angiogenic signaling molecules and their cognate receptors have been identified and characterized [3,4]. Among them, members of the vascular endothelial growth factor (VEGF)/VEGFR family are considered the prime regulators of both physiological and pathological angiogenesis [2]. VEGFR2, which is primarily expressed in vascular endothelium, is a key mediator of VEGF-induced pro-angiogenic activities [5], playing a pivotal role in the regulation of endothelial cell biology [6]. VEGFR2 is upregulated in tumor vasculature compared to normal vasculature [7], thus emerging as an attractive antiangiogenic target.

Many promising new antiangiogenic therapies targeting the VEGF-VEGFR axis with different mechanisms of action have been evaluated in recent years. Examples include VEGFA-specific agents (e.g., bevacizumab, ranibizumab, VEGF-trap), neutralizing VEGFR2-specific antibodies/antibody fragments (e.g., ramucirumab and CDP791), and small molecule tyrosine kinase inhibitors that block VEGFR signaling (e.g., sunitinib, axitinib, sorafenib) (see an overview of clinical studies in [8]).

However, not all patients respond to antiangiogenic therapy [9-11]. It is increasingly evident that the successful implementation of these therapies requires improved diagnostic tools that can identify the patient population that is most likely to respond and match it with the optimal treatment [12]. A noninvasive imaging technique for monitoring the status of tumor angiogenesis that could provide a prompt readout of posttreatment response is therefore highly desirable [13].

For this purpose, imaging agents for single photon emission computed tomography (SPECT) and positron emission tomography (PET) targeting VEGFRs and their ligands could enable a detailed characterization of the molecular status of the endothelium in the tumor.

Efforts to image the VEGF-VEGFR axis have so far been focused either on tracing the ligand distribution with anti-VEGFA monoclonal antibodies or on imaging of VEGFR2 expression using natural/mutated VEGF isoforms. Nagengast et al. were the first to demonstrate the potential of ^{111}In- and ^{89}Zr-labeled bevacizumab for noninvasive in vivo imaging of VEGFA [14]. Bevacizumab was subsequently labeled with iodine-125, yttrium-86 and copper-64 [15-17]. However, imaging of VEGFA is challenging due to its complex and dynamic nature. VEGFA is often sequestered in the extracellular matrix through its interaction with heparan sulfate and is released by proteolytic activity in the tumor microenvironment [18, 19]. Moreover, an important limitation of using monoclonal antibodies as imaging probes is that they circulate in the blood for several days requiring long times after injection to achieve reasonable contrast. In addition, nonspecific uptake of antibodies in tumors due to the enhanced permeability and retention (EPR) effect might lead to false-positive findings and limit therapy monitoring [20]. VEGFA isoforms have also garnered increasing attention as imaging agents during the last two decades. VEGF165 and VEGF121 have been labeled with various radionuclides, such as iodine-123 and -125, copper-64, gallium-68, technetium-99m [21-25], and an engineered single-chain version of VEGFA selective to VEGFR2 (scVR2) has been labeled with zirconium-89 [26], showing encouraging imaging results. However, these findings have been tempered by the inherent angiogenic activity of such agents and the costs associated with their large-scale synthesis.

Affibody molecules are a class of scaffold proteins with short blood circulation time, high stability and high target affinity [27,28]. Recently, Fleetwood et al. reported the selection of several anti-VEGFR2 affibody molecules with affinities to VEGFR2 below 10 nM [29]. Affibody molecules were selected for binding to human VEGFR2 (hVEGFR2) but also demonstrated cross-reactivity to murine VEGFR2 (mVEGFR2) in the low nanomolar range. Although all selected affibody molecules blocked VEGFA-binding to VEGFR2 *in vitro*, they recognized nonoverlapping epitopes on the receptor and could bind simultaneously [29]. Furthermore, they inhibited VEGFA-induced phosphorylation and cell proliferation [30].

Binders with low picomolar affinity are desirable for targets with low expression/density. In the case of HER2 targeting, affibody molecules with an affinity of 160 pM had 6.5-fold higher tumor uptake and 2-fold slower wash-out compared to counterparts with 3.8 nM affinity in tumors with low receptor density (4×10^3 receptors/cell) [31]. We hypothesized that i) the fusion of two anti-VEGFR2 affibody molecules targeting nonoverlapping epitopes (so-called biparatopic dimer) should increase affinity due to the avidity effect by increasing the binding area, and ii)

the increase in protein size should not play a negative role since receptor expression is primarily limited to endothelial cells and tissue penetration is not essential. Here, we used the strategy of fusing two anti-VEGFR2 affibody molecules targeting nonoverlapping epitopes with affinities in the nanomolar range to create a biparatopic affibody dimer denoted Z_{VEGFR2}-Bp_2, which showed increased target affinity. The unique C-terminal cysteine residue enables site-specific conjugation of the NODAGA chelator for labeling with radiometals. In this feasibility study, indium-111 ($t_{½}$ = 2.8 days) was used as the label since it permits the long experiments that are required for accurate characterization of the new binder, e.g., determination of affinity, cellular processing and following the biodistribution profile of the new conjugate at later time points. We show that NODAGA-Z_{VEGFR2}-Bp_2 can be exploited for noninvasive visualization of tumor angiogenesis in preclinical GBM.

Methods

Detailed descriptions of materials, equipment and methods used in this study are given in Supplementary Material.

Production and characterization of anti-VEGFR2 affibody

The new antagonistic biparatopic affibody conjugate was designed and produced in *E. coli* BL21 Star (DE3) cells. Purity and size of the purified protein were analyzed by sodium dodecyl sulfate-polyacrylamide gel electrophoresis (SDS-PAGE) and liquid chromatography-electrospray ionization mass spectrometry (LC-ESI/MS). A maleimide derivative of 1,4,7-triazacyclononane,1-glutaric acid-4,7 acetic acid (NODAGA) was site-specifically conjugated to the unique C-terminal cysteine of the protein. The conjugated protein was purified by semipreparative reversed-phase high-performance liquid chromatography (RP-HPLC). Correct protein mass was confirmed by LC/ESI-MS. The purity of the conjugated protein was determined by analytical RP-HPLC. The secondary structure and thermal stability of the final NODAGA-Z_{VEGFR2}-Bp_2 conjugate (HEHEHE-Z_{VEGFR2}-Bp_2-Cys-Maleimide-NODAGA) were analyzed by circular dichroism (CD) spectroscopy. Binding of the new conjugate was detected by flow-cytometric analysis and by surface plasmon resonance-based biosensor assay.

Radiolabeling and characterization of [^{111}In]In-NODAGA-Z_{VEGFR2}-Bp_2

NODAGA-Z_{VEGFR2}-Bp_2 was incubated with indium-111 in ammonium acetate buffer, pH 5.5, at 85 °C for 30 min. The radiochemical yield of the conjugate in the crude mixture was determined by instant thin layer chromatography (ITLC). The stability of the compound was tested in 1000-fold molar excess of ethylenediaminetetraacetic acid (EDTA) and in PBS at a pH of 7.4. Purification of the radiolabeled conjugate for in vivo studies was performed using size exclusion NAP5-columns. The radiochemical purity was analyzed by radio-ITLC and verified by SDS-PAGE.

In vitro characterization of [^{111}In]In-NODAGA-Z_{VEGFR2}-Bp_2

The temperature-sensitive SV40T-transformed pancreatic islet endothelial cell line Mus EC MS1 mouse endothelial (MS1) used for in vitro characterization was a kind gift from Dr. Jack L. Arbiser, Children's Hospital, Harvard Medical School, Boston, MA [32]. In vitro binding specificity and cellular processing were studied according to published methods [33].

Association to and dissociation of ^{111}In-labeled NODAGA-Z_{VEGFR2}-Bp_2 from VEGFR2 were investigated in MS1 cells by quantitative real-time binding measurements using LigandTracer Yellow Instruments. The resulting data were analyzed in TraceDrawer™ to calculate the association rate (k_a) and dissociation rate (k_d) constants, as well as the dissociation constant K_D.

To estimate if [^{111}In]In-NODAGA-Z_{VEGFR2}-Bp_2 can detect changes in VEGFR2 expression in response to endothelial cell-targeted therapy, in vitro binding of the tracer to MS1 cells treated with heat shock protein 90 (HSP90) inhibitor 17-DMAG (17-dimethylaminoethylamino-17-demethoxygeldanamycin, Alvespimycin) was measured. Untreated cells were used as a control. The results of the binding experiments were correlated with the cell survival fraction, determined as described [34].

Small animal studies

All animal experiments were planned and performed in accordance with national legislation on laboratory animals' protection and were approved by the Ethics Committee for Animal Research in Uppsala.

In vivo stability of [^{111}In]In-NODAGA-Z_{VEGFR2}-Bp_2 was studied in NMRI mice 15 min after intravenous injection of 4 µg (10 MBq) of protein in the tail vein and by comparison of the biodistribution of [^{111}In]In-NODAGA-Z_{VEGFR2}-Bp_2 and [^{111}In]In-acetate 2 h after intravenous injection. Targeting specificity, biodistribution of activity over time and imaging properties of [^{111}In]In-NODAGA-Z_{VEGFR2}-Bp_2 were studied in Balb/c *nu/nu* mice bearing

subcutaneous MS1 tumors. Balb/c nu/nu mice with subcutaneous PC-3 (prostate carcinoma) xenografts were used to verify in vivo targeting of [^{111}In]In-NODAGA-Z_{VEGFR2}-Bp_2 to human VEGFR2. C57BL/6 mice with intracranial GL261 glioblastoma tumors were used to study the imaging properties of [^{111}In]In-NODAGA-Z_{VEGFR2}-Bp_2. Groups of 3-4 mice were used per data point if not stated otherwise.

Mice bearing MS1 tumors were injected intravenously in the tail with 1, 4 and 20 µg of ^{111}In-labeled compound (30 kBq), and biodistribution was studied 2 h post injection (pi). Additionally, biodistribution was studied 6 and 24 h pi with 4 µg of [^{111}In]In-NODAGA-Z_{VEGFR2}-Bp_2 (30 kBq). The PC-3 xenografted mice were injected with 4 µg of [^{111}In]In-NODAGA-Z_{VEGFR2}-Bp_2 (30 kBq), and biodistribution was studied at 2 h pi.

For whole body SPECT/CT imaging, mice bearing MS1 tumors were injected intravenously with 4 µg of [^{111}In]In-NODAGA-Z_{VEGFR2}-Bp_2 (10 MBq). The animals were sacrificed at 2 h pi, and SPECT/CT scans were carried out with a nanoScan SPECT/CT.

Mice with intracranial murine glioblastoma GL261 tumors were monitored under anesthesia on a 3T nanoScan PET/MRI instrument every third day starting from day 12 after tumor inoculation. The mice with MRI-confirmed orthotopic GL261 glioma tumors were injected intravenously with [^{111}In]In-NODAGA-Z_{VEGFR2}-Bp_2 (1-40 µg, 6 MBq/µg). The animals were euthanized at 2 h pi, and SPECT/CT scans were carried out using a nanoScan SPECT/CT as described above. To confirm targeting specificity, an additional group of mice was injected with 4 µg of ^{111}In-labeled Z_{taq}-Z_{taq}.

SPECT raw data were reconstructed using the Tera-Tomo™ 3D algorithm. The CT raw files were reconstructed using Filter Back Projection. SPECT data were reconstructed for attenuation and scatter corrections with their respective CTs. SPECT–CT data were fused and analyzed in PMOD 3.510. SPECT images were presented as MIP (maximum intensity projection) on the RGB color scale, and CT were presented as MIP in grayscale.

For the tumor and cerebellum, spheres of 4 mm radius were drawn on fused SPECT-CT images. Relative uptake of tracer (tumor-to-cerebellum) was evaluated in unmasked whole brain images. Regions of interests (ROIs) were drawn on fused SPECT-CT images along the trans-axial plane to create a mask of the whole brain volume. The whole brain mask was used to exclude pixels outside the selected area to visualize the distribution of activity in the brain among groups. Masking was performed only for visualization of the tumors as MIP.

Data were analyzed with unpaired, two-tailed t-tests to determine if differences were significant ($p<0.05$).

Whole extracted brains were snap-frozen after imaging, and 20 µm sections were cut through the brain. The activity distribution in brain sections was studied using digital macroautoradiography with a Cyclone Storage Phosphor System and was analyzed using OptiQuant image analysis software. The signal intensities in the ROIs in tumor implants and in intact brain were compared. Further sections were processed for H&E staining. Additional brain sections were immunofluorescently stained for VEGFR2 and CD31.

Results

Production and characterization of Z_{VEGFR2}-Bp_2

The Z_{VEGFR2}-Bp_2 protein (see **Figure 1A** for a schematic outline) was produced in *E. coli* and purified using IMAC. After site-specific conjugation of a maleimide derivative of the NODAGA chelator, the resulting protein was purified by semipreparative RP-HPLC. Analysis using RP-HPLC demonstrated a purity of over 96% (**Figure 1B**). Mass determination on LC/ESI-MS showed identical experimental mass compared with the theoretical value, 14,951 kDa (**Figure 1C**). CD spectroscopy demonstrated an alpha-helical content comparable to typical affibody molecules and high refolding capability after heating up to 90 °C (**Figure 1D**). The melting temperature of the new biparatopic affibody conjugate was determined to be 45 °C (**Figure 1E**).

The interaction between NODAGA-Z_{VEGFR2}-Bp_2 and mVEGFR2 was analyzed using a surface plasmon resonance (SPR)-based biosensor assay to verify that conjugation of the NODAGA chelator had no negative influence on the binding to the receptor. The previously studied Z_{VEGFR2}-Bp_2-ABD [30] was included in the assay for comparison. The results from the assay showed similar binding to mVEGFR2 for NODAGA-Z_{VEGFR2}-Bp_2 compared with Z_{VEGFR2}-Bp_2-ABD, which suggested that the NODAGA conjugation did not appreciably affect association/dissociation of the interaction (**Figure S1**).

A flow cytometry-based assay was performed to investigate the ability of Z_{VEGFR2}-Bp_2 to bind to the murine cell lines, MS1 (SV-40 transformed endothelial), PC-3 (prostate cancer) and GL261 (glioblastoma). Z_{VEGFR2}-Bp_2 was produced and purified in fusion with an albumin-binding domain (ABD) to allow detection [30]. Ramucirumab (anti-human VEGFR2 monoclonal antibody) and DC101 (anti-mouse VEGFR2 monoclonal antibody) were included for comparison. Cell binding of

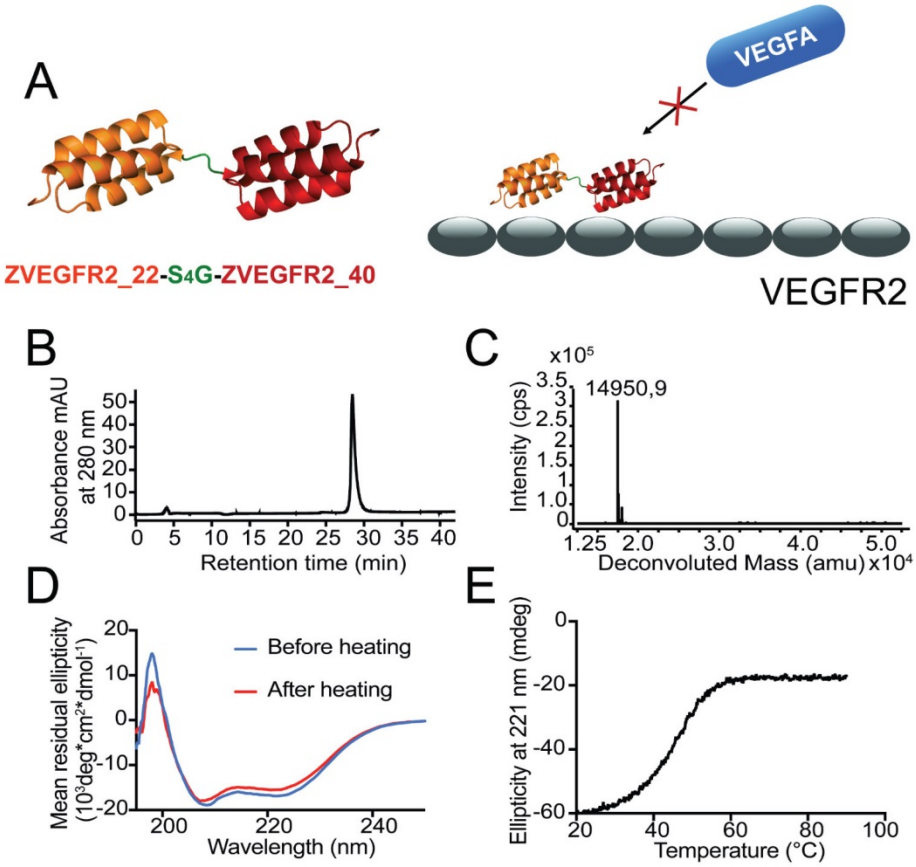

Figure 1. (A) Schematic overview of the design of the dimeric conjugate and the mode of binding of the biparatopic affibody to VEGFR2, blocking the VEGF epitope. **(B)** Purity determination by analytical RP-HPLC for Z_{VEGFR2}-Bp_2. **(C)** LC-ESI/MS mass spectrum for Z_{VEGFR2}-Bp_2. The experimentally determined mass is indicated in the spectrum. **(D)** Determination of refolding capacity. CD spectra before and after heat treatment to 90 °C. **(E)** Determination of heat stability. CD ellipticity at 221 nm as a function of temperature.

Z_{VEGFR2}-Bp_2 was detected using fluorescently labeled human serum albumin (HSA) for Z_{VEGFR2}-Bp_2 and Alexa Fluor® 647 anti-rat or anti-human IgG antibody for Ramucirumab and DC101. A clear shift in the fluorescent signal was observed for the MS1 cell line for both Z_{VEGFR2}-Bp_2 and DC101. For the GL261 and PC-3 cell lines, no significant shift in fluorescence was observed for Z_{VEGFR2}-Bp_2, Ramucirumab or DC101 compared to the negative controls (**Figure 2A**), strongly indicating that these tumor cell lines do not express VEGFR2.

Radiolabeling of NODAGA-Z_{VEGFR2}-Bp_2 with indium-111, identity and stability of [^{111}In]In-NODAGA-Z_{VEGFR2}-Bp_2

NODAGA-Z_{VEGFR2}-Bp_2 was successfully labeled with indium-111 with a radiochemical yield of 97±1% as determined by ITLC (n=34). After size exclusion purification, the radiochemical purity of the product was 100%. SDS-PAGE analysis of the labeled compound showed a single peak well-separated from the low molecular weight control peak represented by the free ^{111}In acetate. Apparent specific activities up to 8.6 MBq/µg (apparent molar activity = 124 GBq/µmol) were obtained. The compound was stable in PBS and in excess EDTA up to 4 h (98±1% of activity associated with protein for PBS and 97±1% for EDTA challenge) (**Table S1**). In blood samples taken 15 min after injection of the tracer in mice, no traces of free indium-111 or ^{111}In-labeled protein fragments were detected (data not shown). Comparison of biodistribution patterns of [^{111}In]In-NODAGA-Z_{VEGFR2}-Bp_2 and free indium-111 2 h after injection (**Figure S2**) showed that the blood clearance of radiolabeled conjugate was much more rapid than for free indium-111, i.e., the activity concentration in blood was 24-fold lower for [^{111}In]In-NODAGA-Z_{VEGFR2}-Bp_2. In contrast, activity uptake in liver was 15-fold lower after injection of free indium-111 than after injection of the radiolabeled conjugate.

In vitro characterization of [^{111}In]In-NODAGA-Z_{VEGFR2}-Bp_2

The *in vitro* binding specificity assay demonstrated specific binding of [^{111}In]In-NODAGA-Z_{VEGFR2}-Bp_2 to VEGFR2-expressing MS1 cells. Presaturation of receptors by adding a large molar excess of non-labeled protein, the natural ligand

VEGF, or the anti-mVEGFR2 antibody DC101 resulted in a significant reduction of cell-associated activity (**Figure 2B**).

[^{111}In]In-NODAGA-Z_{VEGFR2}-Bp_2 was rapidly internalized by MS1 cells (**Figure 2C**). After 8 h of incubation at 37 °C, 55% of cell-associated activity was internalized. Both the cell-associated activity and the internalized fraction plateaued after the 8 h time-point.

The kinetics of [^{111}In]In-NODAGA-Z_{VEGFR2}-Bp_2 binding to VEGFR2 were studied in MS1 cells in real time. The interaction followed a 1:1 Langmuir adsorption model (**Figure 2D**). The calculated dissociation constant at equilibrium was in the low picomolar range (K_D = 3±2 ×10^{-11} M) with a k_a of 8±1 ×10^4 M^{-1}s^{-1} and a k_d of 3±1 ×10^{-6} s^{-1}.

Treatment of endothelial MS1 cells with 17-DMAG was utilized as a model for initial assessment of the potential use of [^{111}In]In-NODAGA-Z_{VEGFR2}-Bp_2 for therapy monitoring. The results showed that continuous incubation of cells with 25 nM 17-DMAG for 14 days resulted in complete cell eradication.

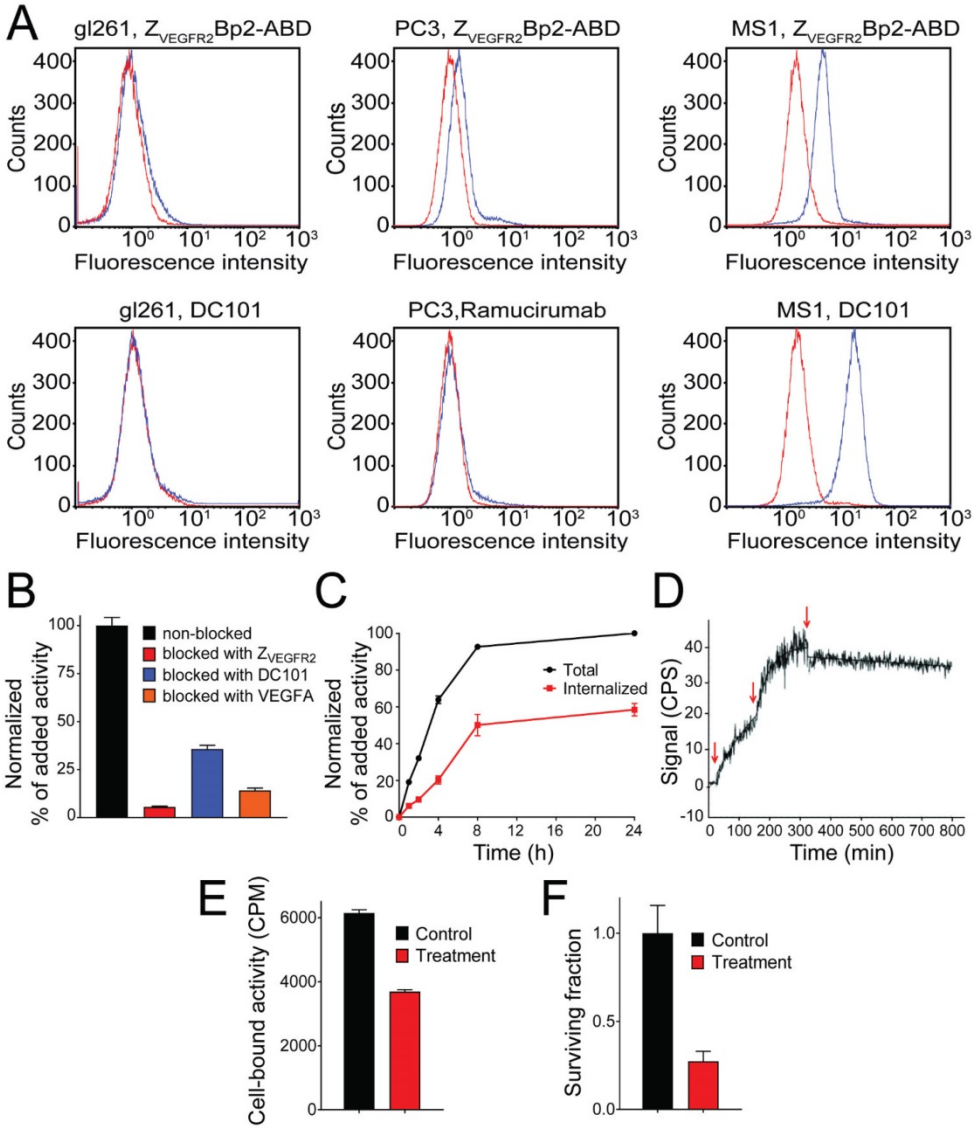

Figure 2. (A) Flow-cytometric analysis of binding of Z_{VEGFR2}-Bp_2 to different cell lines, MS1, PC-3 and GL261. Binding of Z_{VEGFR2}-Bp_2-ABD to cells was detected by Alexa Fluor (AF) 647-labeled HSA. AF-647 labeled HSA was included as negative control. Ramucirumab (anti-hVEGFR2) and DC101 (anti-mVEGFR2) were included as controls for binding to human (PC-3) or mouse (MS1 and GL261) cell lines. Blue histograms indicate affibody/antibody samples, and red histograms are negative controls. The experiment was performed in duplicate. **(B)** In vitro binding specificity of [^{111}In]In-NODAGA-Z_{VEGFR2}-Bp_2 tested on MS1 cells in the presence or absence of non-labeled Z_{VEGFR2}-Bp_2, VEGFA, or anti-mVEGFR2 antibody DC101. The cell-associated activity is presented as a percentage of the total added activity (average value from three cell dishes ± SD). **(C)** Binding and internalization of [^{111}In]In-NODAGA-Z_{VEGFR2}-Bp_2 by MS1 cells. Data are presented as average values from three cell dishes ± SD. Error bars might not be visible because they are smaller than point symbols. **(D)** Real-time binding data of the [^{111}In]In-NODAGA-Z_{VEGFR2}-Bp_2 interaction. Arrows indicate the concentration change. **(E)** Binding of [^{111}In]In-NODAGA-Z_{VEGFR2}-Bp_2 to MS1 cells after 2 h treatment with 25 nM 17-DMAG. An equal amount of cells per culture dish was seeded, and equal [^{111}In]In-NODAGA-Z_{VEGFR2}-Bp_2 activity was added to each cell culture dish. The data are presented as the average value for three cell dishes ± SD. Uptake by treated cells was significantly ($p < 5\times10^{-6}$) lower than by untreated controls. **(F)** Survival of MS1 cells after treatment with 25 nM 17-DMAG over 48 h. The data are presented as the average value for three cell culture flasks ± SD.

Two hours of incubation of MS1 cells with 25 nM 17-DMAG resulted in a significant ($p < 5\times10^{-6}$) decrease in [^{111}In]In-NODAGA-Z_{VEGFR2}-Bp_2 binding (**Figure 2E**). Incubation of MS1 cells with 25 nM 17-DMAG over 48 h resulted in a significant ($p < 0.0001$) decrease in survival compared to untreated control (**Figure 2F**).

Characterization of [^{111}In]In-NODAGA-Z_{VEGFR2}-Bp_2 in small animal models

Targeting properties of [^{111}In]In-NODAGA-Z_{VEGFR2}-Bp_2 were studied in BALB/c *nu/nu* female mice bearing MS1 tumors. Initially, the biodistribution and tumor targeting were studied 2 h pi for three different protein doses: 1, 4 and 20 μg/animal (**Figure 3A** and **Table S2**). The clearance of activity from the blood was efficient for all tested protein doses. There were no significant differences in the biodistribution patterns of activity after the injection of 1 and 4 μg. High activity uptake was found in kidneys, lungs, liver, spleen, and bones. In these organs (except for bones), the activity uptake was dose-dependent. In liver, lungs and spleen, the activity uptake decreased significantly ($p<0.05$) with increased protein dose. Together with the decrease in activity uptake in receptor-expressing organs, the activity uptake increased in kidneys due to more protein being excreted via the renal pathway. The two injected protein doses of 1 and 4 μg provided similar values of tumor uptake. The significantly lower tumor uptake for the 20 μg dose compared to the lower doses indicated partial saturation of VEGFR2 binding and demonstrated in vivo specificity of the radiotracer. Tumor-to-nontumor ratios were higher for the injected protein dose of 4 μg than for 1 μg (**Figure 3B** and **Table S2**). However, for all tested doses, tumor activity uptake did not exceed the uptake in liver, spleen, and kidneys and was similar to the uptake in bones and lungs.

The biodistribution of activity after the injection of 4 μg of [^{111}In]In-NODAGA-Z_{VEGFR2}-Bp_2 was further studied 6 and 24 h pi (**Figure 3C** and **Table S3**). With time, the activity uptake decreased significantly in blood, lung, liver, spleen, and tumors. Simultaneously, the activity uptake increased significantly in the kidney (major excretory organ for affibody molecules). In other studied organs and tissues, the activity uptake was stable over time. Tumor-to-nontumor ratios significantly decreased over time with the exception of tumor-to-blood ratio (**Figure 3D** and **Table S3**). Very low activity uptake was found in brain tissue for all tested protein doses and times after injection.

MicroSPECT/CT imaging of mice bearing MS1 tumors was performed at 2 h pi (**Figure 4A**). Tumors were visualized with prominent contrast. High activity uptake was observed in liver and kidneys as

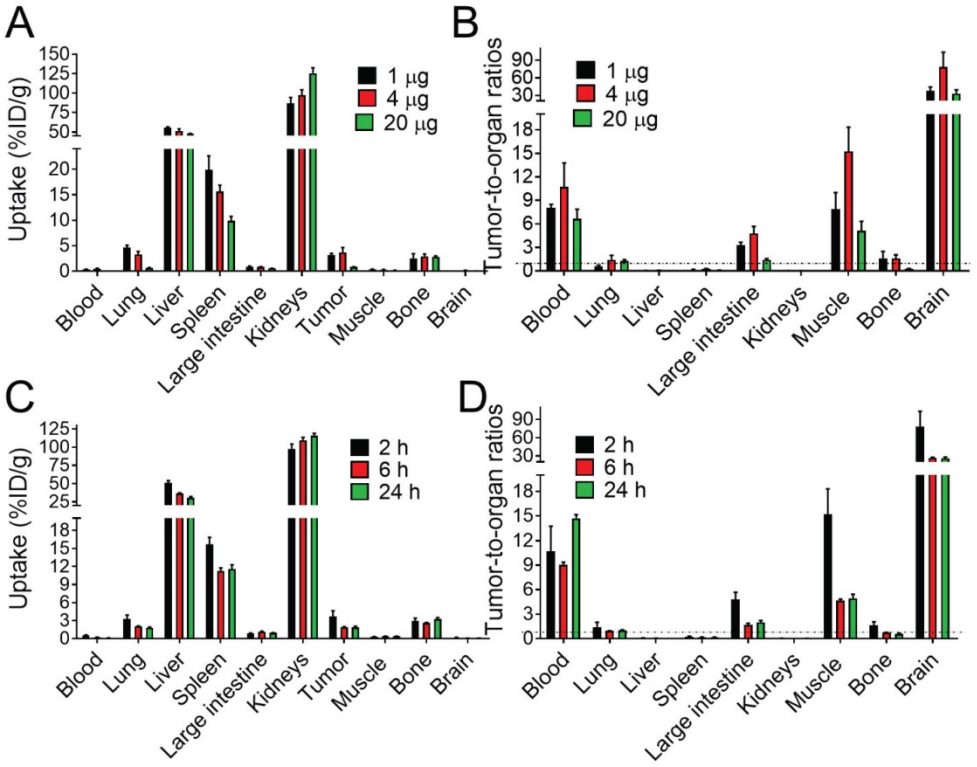

Figure 3. (A, C) Comparative biodistribution of different injected protein doses (1, 4 and 20 μg/animal) of [^{111}In]In-NODAGA-Z_{VEGFR2}-Bp_2 in BALB/C nu/nu in mice bearing MS1 tumors 2 h pi and biodistribution over time 2, 6 and 24 h pi (4 μg/animal). **(B, D)** Tumor-to-normal-tissue ratios 2 h pi (1, 4, 20 μg), 6 h pi (4 μg), and 24 h pi (4 μg).

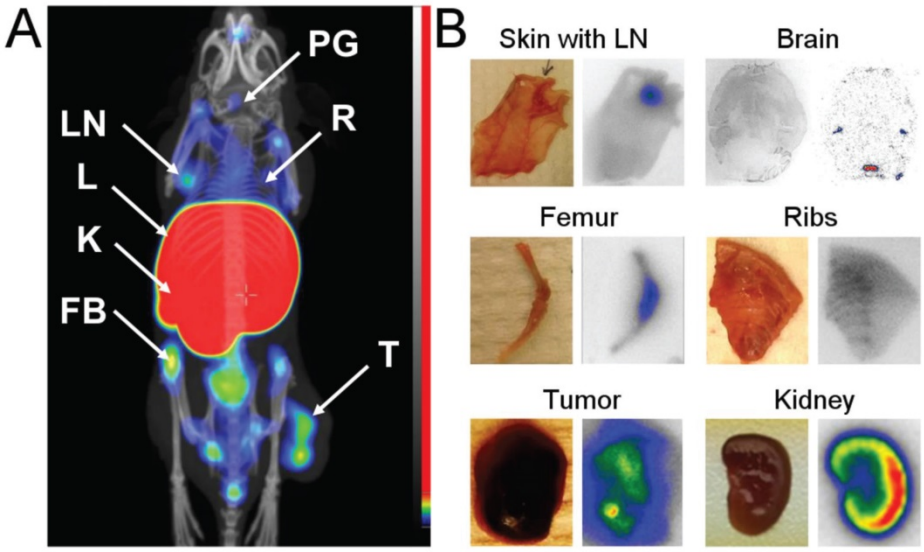

Figure 4. (A) Coronal MIP SPECT/CT images showing tracer distribution in BALB/C nu/nu mice bearing MS1 tumors. The animal used for imaging was injected with 4 μg of [^{111}In]In-NODAGA-Z_{VEGFR2}-Bp_2 and euthanized 2 h pi. LN – lymph node, L – liver, K – kidneys, FB – femur and bone, PG − pineal gland, R – ribs, T – tumor. **(B)** Digital images (right) showing activity distribution detected with macroautoradiography in tissues dissected directly after SPECT/CT imaging.

expected from ex vivo data. The activity uptake in bones was heterogeneous with a higher uptake in the joints. Uptake of activity was also observed in flat bones (sternum, ribs, and hip) and could be assumed in lymph nodes (axillary, inguinal, popliteal, and lymph nodes of head and neck area) and the pineal gland in brain.

To confirm these findings, samples of skin with axillary lymph nodes, breast chest with ribs, femur, kidney, brain and tumor were dissected directly after microSPECT/CT imaging. On autoradiography images (**Figure 4B**), elevated activity uptake was detected in lymph nodes, ribs and joints. The activity uptake in kidneys was concentrated in the cortex. The activity uptake in the pineal gland was confirmed. Additionally, uptake was detected in lateral ventricles. The activity uptake in tumors was heterogeneous, in agreement with the SPECT/CT images.

VEGFR2 targeting was also assessed in mice bearing PC-3 xenografts. Distribution of activity in healthy organs and tissues was in good agreement with the data obtained for the mice bearing MS1 tumors (**Table S4**). However, the activity uptake in tumors of epithelial origin was three-fold lower than for tumors of endothelial origin. This difference translated into lower tumor-to-nontumor ratios for the PC-3 model: tumor-to-blood and tumor-to-muscle, 3; tumor-to-brain, over 20 (**Table S4**).

The growth of intracranial GL261 tumors was monitored using microMRI starting from day 14, when the tumor diameter was approximately 2 mm, to day 21, when the diameter had increased two-fold (**Figure 5A** and **Figure S3**). Activity uptake in intracranial tumors was analyzed as tumor-to-normal brain ratios on microSPECT/CT brain images and on ex vivo autoradiography. Activity uptake in tumors 2 mm in diameter was confirmed by macroautoradiography, but visualization using SPECT was not convincing (**Figure S3**). Based on results from macroautoradiography, the optimal injected protein dose of 4 μg was confirmed (**Figure S4**). It should be noted that according to macroautoradiography data, the activity uptake was more homogeneous in smaller tumors than in tumors with diameters suitable for microSPECT/CT imaging.

Intracranial tumors of 4 mm diameter were visualized on SPECT/CT images (**Figure 5B-C**). In the whole brain masked images, the tumor was easy to delineate when 4 μg of [^{111}In]In-NODAGA-Z_{VEGFR2}-Bp_2 injected (**Figure 5D** and **Figure S5**). The tumor-to-cerebellum ratios after injection of 4 μg [^{111}In]In-NODAGA-Z_{VEGFR2}-Bp_2 were significantly higher than the ratios observed for the 40 μg injected dose and for the non-targeting conjugate (**Figure 5E**).

Microautoradiography of cryosectioned CNS tissue was in good agreement with SPECT/CT images. A high activity uptake was detected in the tumor area (subsequently confirmed by H&E staining) as observed on MRI in the mice injected with 4 μg of [^{111}In]In-NODAGA-Z_{VEGFR2}-Bp_2, and a lower uptake was observed in the mice injected with a blocking amount of targeting or the same dose of non-targeting dimer (**Figure 6A**). H&E staining visualized tumor areas (**Figure 6B**). Tumor-to-brain ratios based on autoradiography results were significantly higher for the mice injected with 4 μg

[^{111}In]In-NODAGA-Z_{VEGFR2}-Bp_2 compared to the tumor-to-brain ratios obtained for the 40 µg injected dose and for the non-targeting conjugate (average for 26-29 slides) (**Figure 6C**). Immunofluorescent staining for the endothelial markers platelet-endothelial cell adhesion molecule-1 (PECAM-1; CD31) and VEGFR2 identified abundant vasculature in the glioblastomas (**Figure 7**), validating the availability of the target.

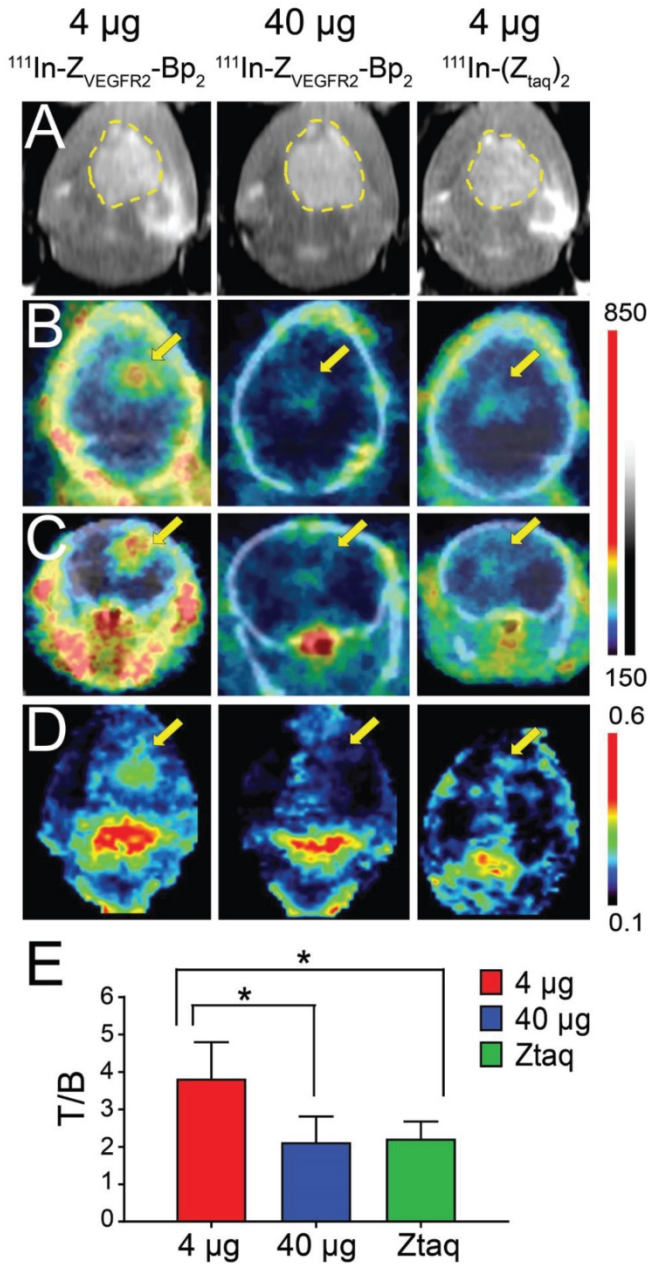

Figure 5. (A) In vivo MRI (prior to the injection) and SPECT/CT **(B)** coronal and **(C)** transaxial imaging of animals with intracranial GL261 tumors at 2 h pi of [^{111}In]In-NODAGA-Z_{VEGFR2}-Bp_2. Animals were injected with 4 µg (left column), 40 µg (middle column) of [^{111}In]In-NODAGA-Z_{VEGFR2}-Bp_2, or 4 µg of [^{111}In]In-NODAGA-Z_{tag}-Z_{taq} (right column). **(D)** Coronal MIP SPECT images showing tracer distribution in the brains of mice bearing intracranial GL261 tumors. For masking, brain VOI was defined using CT images of fused SPECT/CT. The range of the RGB color scale was 0.1-0.6 for Z_{VEGFR2}-Bp_2 and 0.3-0.7 for Z_{tag}-Z_{taq} for comparability. **(E)** Tumor-to-brain ratios based on imaging analysis.

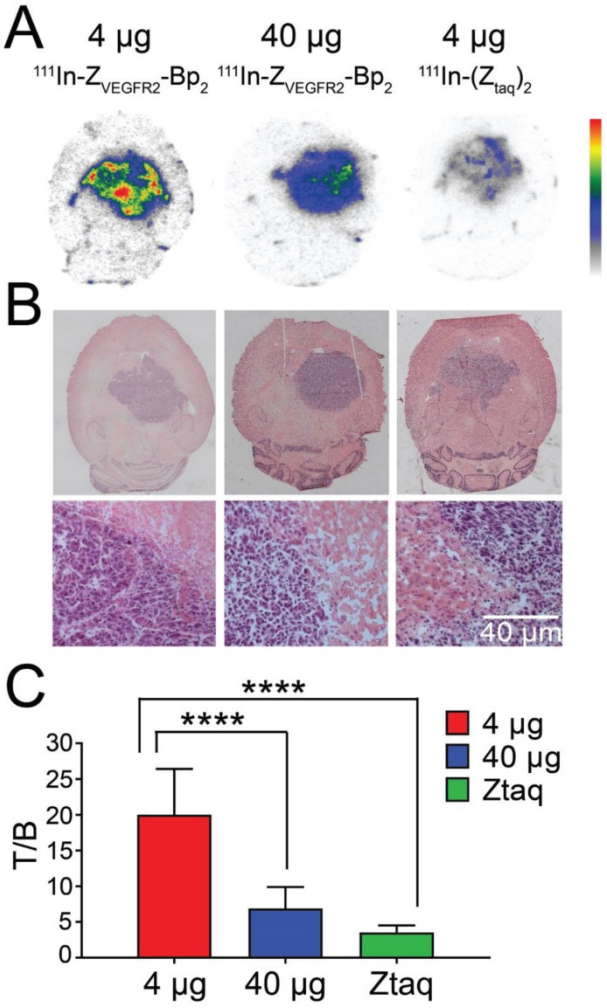

Figure 6. (A) Macroautoradiography and **(B)** H&E staining of brain slices of mice bearing intracranial GL261 tumors. Animals were injected with 4 µg (left column) or 40 µg (middle column) of [^{111}In]In-NODAGA-Z_{VEGFR2}-Bp_2 or 4 µg of [^{111}In]In-NODAGA-Z_{tag}-Z_{taq} (right column) and were euthanized 2 h pi. **(C)** Tumor-to-brain ratios based on macroautoradiography analyses (n = 26-29).

Discussion

Bevacizumab, a VEGFA-targeting antibody blocking ligand binding to VEGFR2, was approved by FDA for recurrent GBM in 2009. It prolongs median progression-free survival after the primary diagnosis and improves progression-free survival and overall survival in after recurrence [9]. However, the assessment of therapeutic effects in GBM and the radiologic evaluation criteria remain challenging and even controversial, in particular distinguishing true progression from treatment-related changes (pseudoprogression or pseudoresponse) [35]. Thus, there is an urgent need for advanced techniques for noninvasive visualization of tumor angiogenesis in GBM to guide therapeutic design and for therapy monitoring. It has been shown in preclinical studies that bevacizumab decreases neovasculature formation, reduces microvessel density, and normalizes vasculature [36]. These effects have also

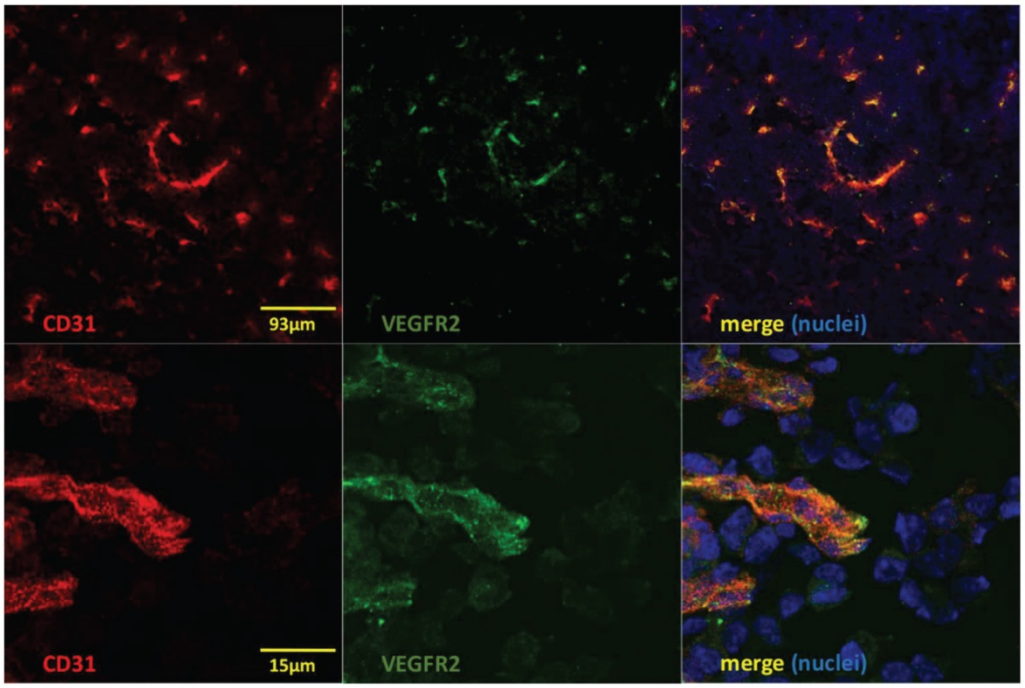

Figure 7. Immunofluorescent staining to detect CD31 (red), VEGFR2 (green) and nuclei (DAPI; blue) shows colocalization of CD31 and VEGFR2 (merged images to the right) on vessel structures in GL261 glioblastomas. Lower panels show high magnification of a region in the upper images.

been observed in GBM patients with decreased VEGFR2 expression during treatment [11,37]. Preclinical and clinical evidence thus point to VEGFR2 expression as a possible predictive or pharmacodynamic biomarker for antiangiogenic therapy in GBM. For example, it was found in a Phase II trial that GBM patients with high VEGF/VEGFR2 ratios (high VEGF and low VEGFR2) had worse outcomes when treated with bevacizumab [10]. Thus, radionuclide molecular imaging of VEGFR2 expression in GBM might provide important diagnostic information and make antiangiogenic therapy of GBM more personalized. It is conceivable that the initial elevated expression would predict response to therapy, and its downregulation during treatment would be a marker of response.

Here, we present the binding affinity and specificity, internalization rate, optimal injected protein dose and optimal imaging window for a new VEGFR2-specific reagent. The properties of this new tool indicate that it has important potential for clinical monitoring of GBM. The labeling of NODAGA-Z_{VEGFR2}-Bp_2 with indium-111 was successful, with high apparent molar activities of up to 124 GBq/µmol that may be required for imaging of targets with low density when limitations on the injected mass of the imaging probe could be an issue [38]. [^{111}In]In-NODAGA-Z_{VEGFR2}-Bp_2 showed excellent stability and retained binding specificity to VEGFR2 in vitro and in vivo. The new binder competed with the binding of the natural ligand VEGFA to VEGFR2, a feature that could be exploited for monitoring of receptor occupancy during antiangiogenic treatment. The potential of VEGFR2 imaging using [^{111}In]In-NODAGA-Z_{VEGFR2}-Bp_2 to predict response to neovasculature-targeted therapy was assessed in vitro using the HSP90 inhibitor 17-DMAG. HSP90 regulates many aspects of tumor angiogenesis, and its inhibition downregulates VEGFR2 expression [39]. Binding of [^{111}In]In-NODAGA-Z_{VEGFR2}-Bp_2 to MS1 cells decreased after treatment with 17-DMAG (**Figure 2E-F**). [^{111}In]In-NODAGA-Z_{VEGFR2}-Bp_2 demonstrated a somewhat higher internalization rate compared to affibody conjugates targeting other tyrosine kinase receptors (e.g., HER2 [33]) that warrants the use of a residualizing radiometal label. Ligand-receptor binding kinetics measured in real-time showed dissociation constant values in the low picomolar range (30 pM). The affinity of [^{111}In]In-NODAGA-Z_{VEGFR2}-Bp_2 for binding to VEGFR2 was two orders of magnitude better than affinities of either parental affibody monomers. This finding corroborates our hypothesis that fusion of two affibody binders with moderate affinity towards different epitopes situated in close proximity should improve the binding affinity of the biparatopic molecule. The low dissociation rate constant of 3×10^{-6} s^{-1} together with the internalization should be beneficial for targets exposed to blood flow where the ligand can be easily cleared if dissociated from the receptor. In conclusion, Z_{VEGFR2}-Bp_2 has properties that indicate that it is particularly well suited for

detection of neovasculature in CNS tumors.

Finding the optimal injected protein dose and the optimal imaging window was the focus of the initial in vivo characterization. The overall biodistribution pattern of the new agent was in good agreement with other VEGFR2-targeting agents ([40-43], as shown particularly in Figure 8 in [44]). The in vivo data showed a pronounced influence of injected protein dose on the imaging contrast (**Figure 3A-B**). The blood clearance of activity was fast, and the tumor-to-blood ratios 2 h pi were approximately 10 for MS1 (endothelial) and 3 for PC-3 (epithelial) tumors, reflecting different target density in a tumor composed of endothelial cells compared to an epithelial tumor with VEGFR2 expression confined to the host-derived tumor vasculature. Remarkably, the tumor-to-blood ratios provided by [^{111}In]In-NODAGA-Z_{VEGFR2}-Bp_2 in both tumor models were superior to ^{64}Cu-labeled ramucirumab (~1 at 48 h pi), $^{61/64}$Cu-labeled VEGF121 (~1 at 8 h pi for ^{61}Cu and ~2 at 16 h pi for ^{64}Cu), ^{68}Ga -labeled VEGF121 (<1 at 4 h pi), and scVR2 (<2 at 2 h pi) [26,40-43]. A high tumor-to-blood ratio is important for imaging. It determines the imaging contrast in vivo as blood-associated activity contributes to activity in all organs.

Increasing the injected protein dose from 1 to 4 μg increased the tumor-to-nontumor ratios, in agreement with earlier studies where the increase of injected affibody mass resulted in increased imaging contrast for ubiquitously expressed molecular targets, e.g., HER1 and HER3 [45,46], likely due to partial saturation of receptors in normal tissues and reduced sequestering of radiolabeled conjugate. High and partially blockable activity uptake was seen in liver, lungs and spleen (**Figure 3A**). This finding could possibly be explained by the low expression of VEGFR2 in epithelial cells. However, a more likely explanation would rest on the assumption that the small size of the affibody probe would allow it to cross the vessel wall, e.g., at endothelial junctions in the peripheral vasculature and to bind to VEGFR2 expressed on the basolateral aspect of the endothelial vessel lining. In contrast, in the CNS, the tight vessel barrier (blood-brain-barrier) would prevent extravasation of the affibody, explaining the better tumor-to-organ ratio observed for glioblastoma compared to brain tissue [47]. Thus, the high uptake in liver, lung and spleen could, to some extent, represent specific binding of the affibody to the vasculature in these organs. It should be noted that the same organs demonstrated high uptake of $^{61/64}$Cu- and ^{68}Ga-labeled VEGFA isoforms, VEGFR121, in earlier studies [41-43].

High activity uptake was also found in kidneys and bones. Bone uptake is most likely due to VEGFR2 expression in the vasculature and on certain leukocyte populations in the red bone marrow [48], while the high kidney uptake could partially reflect the high reabsorption of the affibody conjugate after renal excretion [49]. However, specific binding to VEGFR2 expressed in nonendothelial cell types cannot be ruled out [50].

The high uptake in the liver is particularly challenging for imaging, as the liver is a large and well-perfused organ with a well-fenestrated vasculature. The high capacity for liver entrapment could reduce the bioavailability of the tracer. Therefore, finding the optimal injection dose would be even more challenging.

The overall higher tumor-to-organ ratios for the 4 μg dose in the MS1 model indicate that this dose might be preferred for investigation of biodistribution over time. The relatively rapid washout of activity from the tumor could be explained by dissociation of the affibody-receptor complex despite the strong affinity of Z_{VEGFR2}-Bp_2 to VEGFR2 (low picomolar range). This finding supports our hypothesis that high binding affinity is required for targeting of receptors that are exposed to blood flow. Consequently, the overall tumor-to-organ ratios decreased over time (**Figure 3D**), suggesting that the optimal time point for image acquisition should be shortly after administration. SPECT/CT images acquired 2 h pi with 4 μg [^{111}In]In-NODAGA-Z_{VEGFR2}-Bp_2 were in good agreement with the data obtained in ex vivo measurements (**Figure 4A**). The overall biodistribution pattern indicates that the diagnostic potential of [^{111}In]In-NODAGA-Z_{VEGFR2}-Bp_2, as well as other VEGFR2 binders, will be limited in most cancers due to high uptake in major metastatic sites, such as liver, lungs, lymph nodes and bones.

The tumor-to-normal brain ratios seen for [^{111}In]In-NODAGA-Z_{VEGFR2}-Bp_2 in vivo (~80 at 2 h pi) were much higher than reported for ^{64}Cu-labeled ramucirumab (~10 at 48 h pi) and ^{61}Cu-labeled VEGF121 (~5 at 8 h pi) [40.41], suggesting that the conjugate could be used for VEGFR2 imaging in GBM. For imaging of GBM in a murine model, GL261 was chosen as this glioma model is known to replicate phenotypic characteristics of the human disease, such as invasive growth [51]. Preliminary autoradiography results on brain slides of mice injected with [^{111}In]In-NODAGA-Z_{VEGFR2}-Bp_2 demonstrated low activity uptake in the brain limited to the pineal gland and lateral ventricles (**Figure 4B**). Using SPECT/CT and post-imaging autoradiography in mice bearing GL261 tumors, the optimal injected protein dose (4 μg/mouse) and required tumor size (4 mm in diameter) were verified (**Figure S3** and **Figure S4**).

SPECT/CT images showed a high accumulation of [^{111}In]In-NODAGA-Z_{VEGFR2}-Bp_2 in the area of the brain containing the tumor implants detected in MR images (**Figure 5**). Imaging of VEGFR2 in the orthotopic GBM murine model was VEGFR2-specific considering that both the increase in injected protein dose and the use of non-targeting size-matched affibody conjugate resulted in significantly decreased tumor-to-brain ratios (**Figure 5E**). In SPECT images, tumor-to-cerebellum ratios were two-fold higher for animals injected with 4 μg of [^{111}In]In-NODAGA-Z_{VEGFR2}-Bp_2 compared to animals injected with lower apparent specific activity or a size-matched, non-targeting affibody. The difference in activity uptake in tumors and normal brain tissue was even more pronounced when autoradiograms of brain slices were analyzed: tumor-to-normal brain ratios were three-fold higher for the cohort injected with 4 μg compared to the 40 μg group and six-fold higher compared to the non-targeted group (**Figure 6C**). This discrepancy between SPECT imaging and autoradiography can be explained by several factors: the relatively small size of the tumors that both limited delineation accuracy and contributed to a partial volume effect, heterogeneous activity uptake within tumors, and the limited quantification accuracy of SPECT imaging.

The results of this study demonstrate that our strategy for the development of a high-affinity biparatopic anti-VEGFR2 affibody conjugate by dimerization of two distinct epitope binders was successful. Often, the dimerization of affibody molecules results in decreased tumor uptake. This phenomenon is a consequence of the reduction in tumor penetration that is not compensated by the increased binding affinity and has been observed for anti-HER2 and anti-HER1 affibody molecules [52,53]. However, conceivably, targeting of VEGFR2 does not require deep tissue penetration as the target is located on endothelial cells.

In this study, we demonstrated that the anti-VEGFR2 biparatopic affibody conjugate is potentially suitable for molecular targeting in GBM for patient stratification to antiangiogenic therapies and monitoring of therapy response. In clinical practice, imaging of VEGFR2 expression will not be used for tumor detection, but rather for target detection, concentrating on the areas with already confirmed tumors, e.g., by MRI. Our clinical experience with detection of HER2 expression in breast cancer patients using ^{68}Ga-labeled affibody molecule ABY-025 demonstrated that even tumors with low activity uptake due to low receptor expression can be successfully visualized [54] and that absorbed doses to liver and kidneys were less than the maximum allowed to a single organ in a healthy adult after administration of a clinically relevant amount of gallium-68 [55]. Moreover, the tumor-to-blood and tumor-to-brain ratios for the new imaging tracer were superior to those recorded for the natural ligand to VEGFR2 and anti-VEGFR2 monoclonal antibodies. An additional advantage of affibody-based tracers is the less expensive production by prokaryotic cells [56].

Selection of an optimal imaging strategy is essential for the development of a novel imaging probe. We had to take into account that imaging 24 h or later might provide higher contrast, as has been observed for anti-HER2 affibody molecules [^{111}In]In-ABY-025 [57]. Therefore, the use of some long-lived radionuclide would be desirable for the initial evaluation. Furthermore, advantages of clinical PET over SPECT (better resolution and better attenuation correction providing more accurate quantification) are not valid for small animal scanners. The positron range in tissues results in noticeable degradation of the resolution of small animal PET compared to SPECT. Our scanner, the nanoScan SPECT, has around 2-fold better spatial resolution compared to the nanoScan PET [58,59]. This difference is translated into a smaller partial volume effect in quantitative imaging of small lesions, such as the orthotopic glioblastoma model. The uncertainty in attenuation correction is much lower in preclinical SPECT when the size of the attenuating tissue is much smaller. Dosimetry considerations are not important for small animal imaging, which permits injection of higher activity and compensation for reduced registration efficiency. Therefore, we selected the long-lived single-photon emitter ^{111}In for this initial study.

Our findings indicate that the optimal imaging time window for this agent is shortly after administration. This finding is compatible with the half-life of a short-lived generator-produced positron-emitting gallium-68, thus allowing the use of PET in clinics, which would provide higher imaging sensitivity and more accurate activity quantification. We foresaw such a possibility when designing the tracer. Therefore, we selected the NODAGA chelator, which is suitable for ^{68}Ga as well. NODAGA, a cyclic tri-aza chelator provides stable labeling of peptides and scaffold proteins with ^{68}Ga for PET and ^{111}In for SPECT [60-62]. Some reoptimization of labeling conditions (temperature, pH and time) and preclinical validation should permit the use of [^{68}Ga]Ga-NODAGA-Z_{VEGFR2}-Bp_2 in clinical PET.

Our studies demonstrated that activity concentration in blood was less than 0.5% ID/g, even by 2 h pi for all tested protein doses and appreciably

decreased with time, which was in good agreement with data for other dimeric affibody molecules [52,53], and 15-fold lower than after injection of free indium-111. This finding indicated high in vivo stability of the ^{111}In-NODAGA complex. Possible transchelation of indium-111 to transferrin (the most abundant blood protein with chelating properties) should cause elevated activity concentration in blood with very slow elimination, which was not observed.

Cross-reactivity between murine and human VEGFR2 is critical for clinical translation and has been a focus in the development of the binders from the initial selection of the first-generation candidates [29]. That selection effort yielded two variants that bound human VEGFR2 and were also cross-reactive for murine VEGFR2. After affinity maturation and construction of the biparatopic high-affinity binder (Z_{VEGFR2}-Bp2), we again confirmed cross-reactivity between human VEGR2 and murine VEGFR2 [29,30]. The Z_{VEGFR2}-Bp2 hence binds both orthologs with similar affinity and the affinity measurements presented here are in agreement with the previously published results, indicating a strong position for future clinical translation.

In conclusion, the high-affinity anti-VEGFR2 affibody conjugate [^{111}In]In-NODAGA-Z_{VEGFR2}-Bp_2 specifically targeted VEGFR2 in vivo and visualized VEGFR2 expression in glioblastoma in a murine orthotopic model. Tumor-to-blood ratios for [^{111}In]In-NODAGA-Z_{VEGFR2}-Bp_2 were higher compared to other VEGFR2 imaging probes. [^{111}In]In-NODAGA-Z_{VEGFR2}-Bp_2 appears to be a promising probe for in vivo, noninvasive visualization of tumor angiogenesis in GBM. Further studies should concentrate on the development of imaging probes suitable for PET to evaluate the imaging potential of the new agent, such as therapy monitoring.

Abbreviations

CNS: central nervous system; GBM: glioblastoma multiforme; HER: human epidermal growth factor receptor; %ID/g: percent injected dose per gram; NODAGA: maleimide derivative of 1,4,7-triazacyclononane,1-glutaric acid-4,7 acetic acid; PET: positron emission tomography; SPECT: single photon emission computed tomography; VEGF: vascular endothelial growth factor; VEGFR2: vascular endothelial growth factor receptor-2.

Supplementary Material

Supplementary methods, figures and tables.
http://www.thno.org/v08p4462s1.pdf

Acknowledgements

Dr. Jack L. Arbiser, Children's Hospital, Harvard Medical School, Boston, MA, is acknowledged for the kind gift of the temperature-sensitive SV40T-transformed pancreatic islet endothelial cell line MS1. The authors would also like to thank Marie Hedlund, Department of Immunology, Genetics and Pathology, Uppsala University, for expert technical assistance. The molecular imaging work in this publication was supported by the Wallenberg infrastructure for PET-MRI (WIPPET), a Swedish nationally available imaging platform at Uppsala University, Sweden, financed by Knut and Alice Wallenberg Foundation and Science for Life Laboratory (SciLifeLab pilot infrastructure grant). This work was further supported by the Swedish Cancer Society (grants CAN 2017/649 (JL), CAN2013/586 and CAN 2016/463 (SS), CAN2014/474, CAN 2017/425 (AO), CAN2015/350 (VT), and CAN2016/585 (LCW)), the Swedish Research Council (grants 621-2012-5236 (SS), 2015-02509 (AO), and 2015-02353 (VT)), the Swedish Agency for Innovation VINNOVA (grants 2016-04060 (AO) and 2017-02015 (SS, JL)) and the Wallenberg Center for Protein Technology (SS, JL).

Competing Interests

VT, JL, AO, and SS are the members of the scientific advisory board of Affibody AB. SS, VT and AO are minority share owners of Affibody AB. Affibody AB holds intellectual property rights and trademarks for Affibody molecules. BM, RG, FPR, EL, RKS, FF, SSR, LCW declare no potential conflict of interest.

References

1. Reni M, Mazza E, Zanon S, et al. Central nervous system gliomas. Crit Rev Oncol Hematol. 2017; 113: 213-34.
2. Dvorak HF. Vascular permeability factor/vascular endothelial growth factor: a critical cytokine in tumor angiogenesis and a potential target for diagnosis and therapy. J Clin Oncol. 2002; 20: 4368-80.
3. Claesson-Welsh L. VEGF receptor signal transduction - A brief update. Vascul Pharmacol. 2016; 86: 14-7.
4. Ziyad S, Iruela-Arispe ML. Molecular mechanisms of tumor angiogenesis. Genes Cancer. 2011; 2: 1085-96.
5. Ferrara N. The role of VEGF in the regulation of physiological and pathological angiogenesis. EXS. 2005; 94: 209-31.
6. Simons M, Gordon E, Claesson-Welsh L. Mechanisms and regulation of endothelial VEGF receptor signalling. Nat Rev Mol Cell Biol. 2016; 17: 611-25.
7. Tugues S, Koch S, Gualandi L, et al. Vascular endothelial growth factors and receptors: anti-angiogenic therapy in the treatment of cancer. Mol Aspects Med. 2011; 32: 88-111.
8. Popescu AM, Purcaru SO, Alexandru O, Dricu A. New perspectives in glioblastoma antiangiogenic therapy. Contemp Oncol (Pozn). 2016; 20: 109-18.
9. Diaz RJ, Ali S, Qadir MG, et al. The role of bevacizumab in the treatment of glioblastoma. J Neurooncol. 2017; 133: 455-67.
10. Raizer JJ, Grimm S, Chamberlain MC, et al. A phase 2 trial of single-agent bevacizumab given in an every-3-week schedule for patients with recurrent high-grade gliomas. Cancer. 2010; 116: 5297-305.

11. Castro BA, Flanigan P, Jahangiri A, et al. Macrophage migration inhibitory factor downregulation: a novel mechanism of resistance to anti-angiogenic therapy. Oncogene. 2017; 36: 3749-59.
12. Murukesh N, Dive C, Jayson GC. Biomarkers of angiogenesis and their role in the development of VEGF inhibitors. Br J Cancer. 2010; 102:8-18.
13. Tolmachev V, Stone-Elander S, Orlova A. Radiolabelled receptor-tyrosine-kinase targeting drugs for patient stratification and monitoring of therapy response: prospects and pitfalls. The Lancet Oncology, 2010; 11: 992-1000.
14. Nagengast WB, de Vries EG, Hospers GA, et al. In vivo VEGF imaging with radiolabeled bevacizumab in a human ovarian tumor xenograft. J Nucl Med. 2007; 48: 1313-9.
15. Stollman TH, Scheer MG, Leenders WP, et al. Specific imaging of VEGF-A expression with radiolabeled anti-VEGF monoclonal antibody. Int J Cancer. 2008; 122: 2310-4.
16. Nayak TK, Garmestani K, Baidoo KE, et al. PET imaging of tumor angiogenesis in mice with VEGF-A-targeted (86)Y-CHX-A"-DTPA-bevacizumab. Int J Cancer. 2011; 128: 920-6.
17. Paudyal B, Paudyal P, Oriuchi N, et al. Positron emission tomography imaging and biodistribution of vascular endothelial growth factor with 64Cu-labeled bevacizumab in colorectal cancer xenografts. Cancer Sci. 2011; 102: 117-21.
18. Houck KA, Leung DW, Rowland AM, et al. Dual regulation of vascular endothelial growth factor bioavailability by genetic and proteolytic mechanisms. J Biol Chem. 1992; 267: 26031-7.
19. Wijelath ES, Murray J, Rahman S, et al. Novel vascular endothelial growth factor binding domains of fibronectin enhance vascular endothelial growth factor biological activity. Circ Res. 2002; 91: 25-31.
20. Wester HJ, Kessler H. Molecular targeting with peptides or peptide-polymer conjugates: just a question of size? J Nucl Med. 2005; 46: 1940-5.
21. Li S, Peck-Radosavljevic M, Koller E, et al. Characterization of (123)I-vascular endothelial growth factor-binding sites expressed on human tumour cells: possible implication for tumour scintigraphy. Int J Cancer. 2001; 91: 789–96.
22. Yoshimoto M, Kinuya S, Kawashima A, et al. Radioiodinated VEGF to image tumor angiogenesis in a LS180 tumor xenograft model. Nucl Med Biol. 2006; 33: 963-9.
23. Cai W, Chen K, Mohamedali KA, et al. PET of vascular endothelial growth factor receptor expression. J Nucl Med. 2006; 47: 2048-56.
24. Kang CM, Kim SM, Koo HJ, et al. In vivo characterization of 68Ga-NOTA-VEGF 121 for the imaging of VEGF receptor expression in U87MG tumor xenograft models. Eur J Nucl Med Mol Imaging. 2013; 40: 198-206.
25. Blankenberg FG, Mandl S, Cao YA, et al. Tumor imaging using a standardized radiolabeled adapter protein docked to vascular endothelial growth factor. J Nucl Med. 2004; 45: 1373–80.
26. Meyer JP, Edwards KJ, Kozlowski P, et al. Selective Imaging of VEGFR-1 and VEGFR-2 Using 89Zr-Labeled Single-Chain VEGF Mutants. J Nucl Med. 2016; 57: 1811-6.
27. Tolmachev V, Orlova A, Nilsson FY, et al. Affibody molecules: potential for in vivo imaging of molecular targets for cancer therapy. Expert Opin Biol Ther. 2007; 7: 555-68.
28. Ståhl S, Gräslund T, Eriksson Karlström A, et al. Affibody Molecules in Biotechnological and Medical Applications. Trends Biotechnol. 2017;35: 691-712.
29. Fleetwood F, Klint S, Hanze M, et al. Simultaneous targeting of two ligand-binding sites on VEGFR2 using biparatopic Affibody molecules results in dramatically improved affinity. Sci Rep. 2014; 4: 7518.
30. Fleetwood F, Güler R, Gordon E, et al. Novel affinity binders for neutralization of vascular endothelial growth factor (VEGF) signaling. Cell Mol Life Sci. 2016; 73: 1671-83.
31. Tolmachev V, Tran TA, Rosik D, et al. Tumor targeting using Affibody molecules: an interplay of a target expression level, affinity and binding site composition. J Nucl Med. 2012; 53: 953-60.
32. Arbiser JL, Moses MA, Fernandez CA, et al. Oncogenic H-ras stimulates tumor angiogenesis by two distinct pathways. Proc Natl Acad Sci U S A. 1997; 94: 861-6.
33. Wållberg H, Orlova A. Slow internalization of anti-HER2 synthetic Affibody monomer 111In-DOTA-Zher2:342-pep2: Implications for development of labeled tracers. Cancer Biother Radiopharm. 2008; 23: 435-42.
34. Andersson J, Rosestedt M, Asplund V, et al. In vitro modeling of HER2-targeting therapy in disseminated prostate cancer. Int J Oncol. 2014; 45: 2153-8.
35. Delgado-López PD, Riñones-Mena E, Corrales-García EM. Treatment-related changes in glioblastoma: a review on the controversies in response assessment criteria and the concepts of true progression, pseudoprogression, pseudoresponse and radionecrosis. Clin Transl Oncol. 2018 Aug; 20: 939-53.
36. Yamashita-Kashima Y, Fujimoto-Ouchi K, Yorozu K, et al. Biomarkers for antitumor activity of bevacizumab in gastric cancer models. BMC Cancer. 2012; 12: 37.
37. Stadlbauer A, Zimmermann M, Oberndorfer S, et al. Vascular Hysteresis Loops and Vascular Architecture Mapping in Patients with Glioblastoma treated with Antiangiogenic Therapy. Sci Rep. 2017; 7: 8508.
38. Lee CM, Farde L. Using positron emission tomography to facilitate CNS drug development. Trends Pharmacol Sci. 2006; 27: 310-6.
39. Sanderson S, Valenti M, Gowan S, et al. Benzoquinone ansamycin heat shock protein 90 inhibitors modulate multiple functions required for tumor angiogenesis. Mol Cancer Ther. 2006; 5: 522-32.
40. Luo H, England CG, Graves SA, et al. PET Imaging of VEGFR-2 Expression in Lung Cancer with 64Cu-Labeled Ramucirumab. J Nucl Med. 2016; 57: 285-90.
41. Zhang Y, Hong H, Niu G, et al. Positron emission tomography imaging of vascular endothelial growth factor receptor expression with (61)Cu-labeled lysine-tagged VEGF121. Mol Pharm. 2012; 9: 3586-94.
42. Lee I, Yoon KY, Kang CM, et al. Evaluation of the angiogenesis inhibitor KR-31831 in SKOV-3 tumor-bearing mice using (64)Cu-DOTA-VEGF(121) and microPET. Nucl Med Biol. 2012; 39: 840-6.
43. Kang CM, Koo HJ, Choe YS, et al. ^{68}Ga-NODAGA-VEGF$_{121}$ for in vivo imaging of VEGF receptor expression. Nucl Med Biol. 2014; 41: 51-7.
44. Chen K, Li Z-B, Wang H, et al. Dual-modality optical and positron emission tomography imaging of vascular endothelial growth factor receptor on tumor vasculature using quantum dots. Eur J Nucl Med Mol Imaging. 2008; 35: 2235–44.
45. Tolmachev V, Rosik D, Wållberg H, et al. Imaging of EGFR expression in murine xenografts using site-specifically labelled anti-EGFR 111In-DOTA-Z EGFR:2377 Affibody molecule: aspect of the injected tracer amount. Eur J Nucl Med Mol Imaging. 2010; 37: 613-22.
46. Rosestedt M, Andersson KG, Mitran B, et al. Affibody-mediated PET imaging of HER3 expression in malignant tumours. Sci Rep. 2015; 5: 15226.
47. Zhao Z, Nelson AR, Betsholtz C, Zlokovic BV. Establishment and dysfunction of the blood-brain barrier. Cell. 2015; 163: 1064-78.
48. Hooper AT, Butler JM, Nolan DJ, et al. Engraftment and reconstitution of hematopoiesis is dependent on VEGFR2-mediated regeneration of sinusoidal endothelial cells. Cell Stem Cell. 2009; 4: 263-74.
49. Feldwisch J, Tolmachev V. Engineering of affibody molecules for therapy and diagnostics. Methods Mol Biol. 2012; 899: 103-26.
50. Miettinen M, Rikala M-S, Rysz J, et al. Vascular endothelial growth factor receptor 2 (VEGFR2) as a marker for malignant vascular tumors and mesothelioma – immunohistochemical study of 262 vascular endothelial and 1640 nonvascular tumors. Am J Surg Pathol. 2012; 36: 629–39..
51. Szatmari T, Lumniczky K, Desaknai S, et al. Detailed characterization of the mouse glioma 261 tumor model for experimental glioblastoma therapy. Cancer Sci. 2006; 97: 546-53.
52. Orlova A, Magnusson M, Eriksson TL, et al. Tumor imaging using a picomolar affinity HER2 binding affibody molecule. Cancer Res. 2006; 66: 4339-48.
53. Tolmachev V, Friedman M, Sandström M, et al. Affibody molecules for EGFR targeting in vivo: aspects of dimerization and labeling chemistry. J Nucl Med. 2009; 50: 274-83.
54. Sörensen J, Velikyan I, Sandberg D, et al. Measuring HER2-receptor expression in metastatic breast cancer using [(68)Ga]ABY-025 affibody PET/CT. Theranostics. 2016; 6: 262-71.
55. Sandström M, Lindskog K, Velikyan I, et al. Biodistribution and radiation dosimetry of the anti-HER2 Affibody molecule 68Ga-ABY-025 in breast cancer patients. J Nucl Med. 2016; 57: 867-71.
56. Sanchez-Garcia L, Martín L, Mangues R, et al. Recombinant pharmaceuticals from microbial cells: a 2015 update. Microb Cell Fact. 2016; 15: 33.
57. Ahlgren S, Orlova A, Wållberg H, et al. Targeting of HER2-expressing tumors using 111In-ABY-025, a second-generation affibody molecule with a fundamentally reengineered scaffold. J Nucl Med. 2010; 51: 1131-8.
58. Nagy K, Tóth M, Major P, et al. Performance evaluation of the small-animal nanoScan PET/MRI system. J Nucl Med. 2013; 54: 1825-32.
59. Deleye S1, Van Holen R, Verhaeghe J, et al. Performance evaluation of small-animal multipinhole µSPECT scanners for mouse imaging. Eur J Nucl Med Mol Imaging. 2013; 40: 744-58.
60. Eisenwiener KP, Prata MI, Buschmann I, et al. NODAGATOC, a new chelator-coupled somatostatin analogue labeled with [67/68Ga] and [111In] for SPECT, PET, and targeted therapeutic applications of somatostatin receptor (hsst2) expressing tumors. Bioconjug Chem. 2002; 13: 530-41.

61. Roosenburg S, Laverman P, Joosten L, et al. PET and SPECT imaging of a radiolabeled minigastrin analogue conjugated with DOTA, NOTA, and NODAGA and labeled with (64)Cu, (68)Ga, and (111)In. Mol Pharm. 2014; 11: 3930-7.
62. Strand J, Honarvar H, Perols A, et al. Influence of macrocyclic chelators on the targeting properties of (68)Ga-labeled synthetic affibody molecules: comparison with (111)In-labeled counterparts. PLoS One. 2013; 8: e70028.